J. Fluid Mech. (1998), *vol.* 362, *pp.* 53–82. Printed in the United Kingdom

Numerical simulations of large-amplitude internal solitary waves

By DMITRY E. TEREZ[1] AND OMAR M. KNIO[2]

[1]Department of Earth and Planetary Sciences, The Johns Hopkins University, Baltimore, MD 21218, USA

[2]Department of Mechanical Engineering, The Johns Hopkins University, Baltimore, MD 21218, USA

(Received 27 November 1996 and in revised form 25 November 1997)

A numerical model based on the incompressible two-dimensional Navier–Stokes equations in the Boussinesq approximation is used to study mode-2 internal solitary waves propagating on a pycnocline between two deep layers of different densities. Numerical experiments on the collapse of an initially mixed region reveal a train of solitary waves with the largest leading wave enclosing an intrusional 'bulge'. The waves gradually decay as they propagate along the horizontal direction, with a corresponding reduction in the size of the bulge. When the normalized wave amplitude, a, falls below the critical value $a_c = 1.18$, the wave is no longer able to transport mixed fluid as it propagates away from the mixed region, and a sharp-nosed intrusion is left behind. The wave structure is studied using a Lagrangian particle tracking scheme which shows that for small amplitudes the bulges have a well-defined elliptic shape. At larger amplitudes, the bulge entrains and mixes fluid from the outside while instabilities develop in the rear part of the bulge. Results are obtained for different wave amplitudes ranging from small-amplitude 'regular' waves with $a = 0.7$ to highly nonlinear unstable waves with $a = 3.8$. The dependence of the wave speed and wavelength on amplitude is measured and compared with available experimental data and theoretical predictions. Consistent with experiments, the wave speed increases almost linearly with amplitude at small values of a. As a becomes large, the wave speed increases with amplitude at a smaller rate, which gradually approaches the asymptotic limit for a two-fluid model. Results show that in the parameter range considered the wave amplitude decreases linearly with time at a rate inversely proportional to the Reynolds number. Numerical experiments are also conducted on the head-on collision of solitary waves. The simulations indicate that the waves experience a negative phase shift during the collision, in accordance with experimental observations. Computations are used to determine the dependence of the phase shift on the wave amplitude.

1. Introduction

Internal solitary waves are frequently observed in a variety of atmospheric and oceanic phenomena. In the atmosphere, for example, solitary waves can be generated by thunderstorm outflows, mid-latitude cold fronts or tropical sea-breeze fronts etc. Perhaps the most impressive example of an atmospheric internal solitary wave is the 'morning glory' phenomenon observed in northern Australia (Christie 1992; Clarke,

Smith & Reid 1981; Reeder *et al.* 1995). Numerous observations of internal solitary waves in the ocean are also reported (see e.g. Ostrovsky & Stepanyants 1989; Apel 1981).

This paper focuses on deep-water mode-2 internal solitary waves propagating on a thin continuously stratified pycnocline between two deep layers of different densities. These waves can be easily reproduced in the laboratory and quite a few experiments have been performed with this type of wave, starting with the early work of Davis & Acrivos (1967). In laboratory experiments, internal solitary waves are usually generated by a collapsing mixed fluid region (Maxworthy 1980, 1983; Amen & Maxworthy 1980; Kao & Pao 1980) or by pushing some mass of a mixed fluid along a pycnocline (Davis & Acrivos 1967; Hurdis & Pao 1975; Kamachi & Honji 1982; Stamp & Jacka 1995). Both of these generation techniques produce a persistent internal solitary wave or a train of waves, which propagate a long distance before losing their identity.

Experimental evidence indicates that small-amplitude weakly nonlinear internal solitary waves behave like 'regular' waves, that is, they carry energy and momentum but do not carry mass. In contrast, large-amplitude waves trap some fluid inside and transport it over a long distance (Davis & Acrivos 1967); thus, these waves exhibit some features of gravity currents. In fact, the collapse of a mixed region into a stably stratified environment produces an intrusive gravity current. The head of the gravity current may then separate from the rest of the intrusion, leading to the formation of a highly nonlinear large-amplitude solitary wave, or 'bulge', carrying mixed fluid inside.

Analytical studies of internal solitary waves in deep water have dealt exclusively with weakly nonlinear waves having open streamlines in the frame of reference moving with the wave. Early work on this subject dates back to the studies of Benjamin (1967) and Davis & Acrivos (1967). Both studies construct a governing equation which reflects a balance between nonlinear and dispersive terms and admits soliton solutions.

Analytical weakly nonlinear approaches to 'deep-water' internal solitary waves are typically based on the assumption of a long wave, that is, that the wavelength is much larger than the thickness of the pycnocline. This assumption allows reduction of the partial differential equation to an ordinary one. The analysis also assumes that the wave amplitude is small relative to the pycnocline thickness, which makes perturbation analysis possible. Unfortunately, large-amplitude waves which contain regions of closed streamlines and entrap fluid cannot generally be described by a global separation-of-variables analysis, which underpins all analytical approaches undertaken so far. The difficulties of extending the weakly nonlinear approach to large-amplitude waves were in fact emphasized by Benjamin (1967), who noted that the situation 'offers small hope of any general analytical treatment' and that a 'direct numerical solution of the unsimplified governing equations is likely to be more rewarding'.

One can identify two major approaches to numerical modelling of internal solitary waves. The first is based on finding an inviscid steady-state solution for a single solitary wave in a reference frame moving with the wave. The solution is usually based on integrating the simplified equation derived by Long (1953) for steady-state incompressible inviscid non-diffusive flow of a stratified fluid (Davis & Acrivos 1967; Tung, Chan & Kubota 1982; Brown & Christie 1994*a*). It should be noted, however, that the determination of inviscid steady-state solutions using Long's equation is also faced with several difficulties. In particular, the appearance of recirculation

zones at large wave amplitudes invalidates the assumption of continuous streamlines with known upstream conditions, on which Long's equation is based. While it is possible to make a reasonable approximation for the density distribution within the recirculating region (for example, a uniform density), the inviscid treatment is still faced with the difficulty of specifying or determining the vorticity structure within the bulge. Nonetheless, it is remarkable that despite these difficulties the approach yields wave speed and wavelength predictions that are in close agreement with experimental observations (Tung *et al.* 1982; Stamp & Jacka 1995). Thus, it appears that the details of the wave internal structure do not have a pronounced effect on the large-scale motion of the wave, and that the global wave properties are in large part governed by the size of the bulge.

An alternative to the steady-state inviscid approach is based on direct numerical simulation of incompressible Navier–Stokes equations for stratified flow (e.g. Saffarinia & Kao 1996). While it is more elaborate and demanding than inviscid stready-state models, the numerical simulation approach offers significant advantages. In particular, it naturally extends to large-amplitude waves without the need for simplifying assumptions. In addition, numerical simulations enable us to deduce global properties of internal solitary waves such as wave speed and wavelength, and to perform a detailed examination of their internal structure. Since the internal wave structure is of primary interest to the present study, the numerical simulation approach will be adopted in the analysis.

1.1. *Scope*

Despite the large number of laboratory experiments performed so far, there still exist a number of questions regarding the internal structure of solitary bulges, the behavior of the wave speed and wavelength for large-amplitude waves, and the characteristics of the collision between solitary waves of equal or different amplitudes.

For example, the streak photographs recorded by Kamachi & Honji (1982) using a moving camera reveal that the internal circulation within large-amplitude bulges corresponds to a vortex pair. The presence of counter-rotating cells is also noted in the recent experiments of Stamp & Jacka (1995). On the other hand, some experimental studies of internal solitary waves do not specifically mention the occurrence of counter-rotating cells (e.g. Kao & Pao 1980; Maxworthy 1980), and it is not clear whether these structures do not occur in the corresponding experiments, are very weak or not detected. It is interesting to note, however, that the occurrence of counter-rotating cells within the bulges has been observed in experiments using the acceleration of fluid as a wave generation procedure, whereas experiments relying on the collapse of a mixed region generally do not mention the presence of such cells. Thus, one possibility is that bulges of different types can be generated and that the wave generation procedure determines the type of the bulge actually observed. At the same time, experimental observations clearly indicate that internal solitary waves generated using different initiation mechanisms still share many properties in common. In particular, the dependence of wave speed and wavelength on amplitude appears to be essentially independent of the wave generation mechanism. Consequently, results of our numerical investigation of basic wave parameters are relevant to both scenarios.

One of the objectives of the computational study is a thorough investigation of the wave speed–amplitude dependence for a wide range of wave amplitudes. A detailed comparison of our computed results with available experimental data, analytical weakly nonlinear theory and asymptotic two-fluid solution is performed.

An interesting property of large-amplitude bulges is their apparent ability to entrain

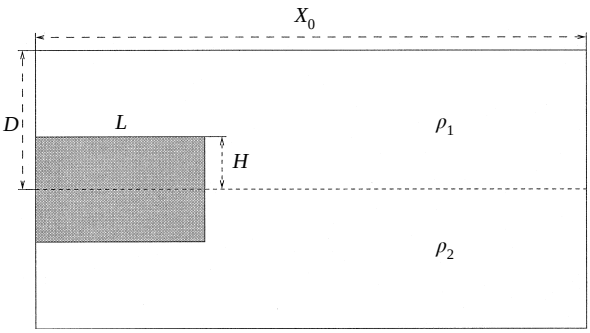

FIGURE 1. The initial configuration in the numerical simulations. Large-amplitude solitary waves are produced by a collapsing mixed region of height H and length L in a long, deep channel. The undisturbed density distibution in the channel is described by a hyperbolic tangent profile (2.1).

and mix fluid from the outside, and to promote local mixing. At present, there exists little evidence regarding these phenomena, whose occurrence has been inferred based on visual observations of dye particles (Stamp & Jacka 1995). To our knowledge, there is little or no information regarding entrainment mechanisms and mixing patterns associated with large-amplitude bulges. Thus, the computations will also be used to investigate their occurrence.

Finally, numerical experiments on the head-on collision of solitary waves are presented. The motivation behind these computational experiments concerns experimental observations which imply that solitary waves experience a negative phase shift during the collision (e.g. Kao & Pao 1980; Stamp & Jacka 1995). However, the magnitude of the phase shift has proven to be extremely difficult to determine accurately from the experimental data. Thus, the computations also aim at determining the magnitude of the phase shift and exploring its dependence on wave amplitude.

2. Formulation

2.1. *Setup and computational domain*

The basic configuration for most of our numerical experiments is shown in figure 1. It represents a two-dimensional channel of length $\tilde{X}_0$ and depth $2\tilde{D}$. (Tildes are used to represent dimensional quantities). The upper half of the channel is filled with fluid of density $\tilde{\rho}_1$ and the lower half has density $\tilde{\rho}_2$; the density difference $\Delta\tilde{\rho} = (\tilde{\rho}_2 - \tilde{\rho}_1)$ is assumed to be relatively small. A continuously stratified pycnocline region is located at the centreline ($z = 0$) and has a characteristic thickness $2\tilde{h}$. The density stratification around the centreline is described by

$$\tilde{\rho}(z) = \tilde{\rho}_0 \left[1 - \frac{\Delta\tilde{\rho}}{2\tilde{\rho}_0} \tanh\left(\frac{\tilde{z}}{\tilde{h}}\right)\right]. \tag{2.1}$$

Large-amplitude solitary waves result from the collapse of a mixed fluid region of density $\tilde{\rho}_0 \equiv (\tilde{\rho}_1 + \tilde{\rho}_2)/2$, length $\tilde{L}$ and height $2\tilde{H}$. The mixed fluid region is assumed to be centred at the origin of a Cartesian (x, z) system, and symmetric about the centreline. The present study focuses on mode-2 internal solitary waves resulting from this symmetric arrangement in the Boussinesq approximation. Only the upper half of the computational domain is involved in the unsteady computations.

Similar setups are used in various laboratory experiments on internal solitary waves

on a pycnocline (e.g. Stamp & Jacka 1995; Davis & Acrivos 1967; and others). This provides us with a well-established basis for comparison and validation purposes.

2.2. *Governing equations and boundary conditions*

To study the evolution of internal solitary waves, or bulges, generated by the collapsing mixed region, we rely on a vorticity-based formulation of the Navier–Stokes and density advection equations for incompressible two-dimensional viscous diffusive flow in the Boussinesq limit. In normalized form, the governing equations are expressed as

$$\frac{\partial \omega}{\partial t} + \frac{\partial (\omega u)}{\partial x} + \frac{\partial (\omega v)}{\partial z} = -\frac{1}{Fr^2}\frac{\partial \rho}{\partial x} + \frac{1}{Re}\nabla^2 \omega, \tag{2.2}$$

$$\frac{\partial \rho}{\partial t} + \frac{\partial (\rho u)}{\partial x} + \frac{\partial (\rho v)}{\partial z} = \frac{1}{ReSc}\nabla^2 \rho, \tag{2.3}$$

$$\nabla^2 \psi = -\omega, \tag{2.4}$$

where $\boldsymbol{u} = (u, v)$ is the normalized velocity vector, $\omega \equiv \nabla \times \boldsymbol{u}$ is the normalized vorticity, and ρ the normalized density anomaly. Variables are normalized with respect to the appropriate combination of characteristic velocity $\tilde{U}_c$, characteristic length $\tilde{l}_c$, and characteristic density $\tilde{\rho}_c$. We choose the undisturbed pycnocline half-thickness, $\tilde{h}$, as reference length, the density difference, $\Delta\tilde{\rho}$, as reference density scale, and use the celerity of a long infinitesimal mode-2 wave in the system as characteristic velocity. Thus, we set

$$\tilde{U}_c = \frac{1}{2}\left(\tilde{g}\tilde{h}\frac{\Delta\tilde{\rho}}{\tilde{\rho}_0}\right)^{1/2} \tag{2.5}$$

where $\tilde{g}$ is the gravitational acceleration. With this choice of reference parameters, the normalized density anomaly is given by

$$\rho = \frac{\tilde{\rho} - \tilde{\rho}_0}{\Delta\tilde{\rho}}. \tag{2.6}$$

The normalization process leads to the definition of three dimensionless parameters: the Froude number Fr, the Reynolds number, $Re \equiv \tilde{U}_c\tilde{h}/\tilde{\nu}$, and the Schmidt number, $Sc \equiv \tilde{\nu}/\tilde{\kappa}$, where $\tilde{\kappa}$ is the mass diffusivity. Also note that, for our choice of reference velocity (2.5) the Froude number in equation (2.2) $Fr = 0.5$.

The boundary conditions used in the computations are as follows. As mentioned earlier, we take advantage of the symmetry of the (Boussinesq) flow and only compute the solution for the upper part of the flow (figure 1). Thus, on the centreline of the channel ($z = 0$) the symmetry boundary condition is applied:

$$\psi = 0, \quad \omega = 0, \quad \rho = 0. \tag{2.7}$$

The left-hand boundary of the domain, $x = 0$, is treated as a 'slip' plane, with the symmetry conditions

$$\psi = 0, \quad \omega = 0, \quad \frac{\partial \rho}{\partial x} = 0. \tag{2.8}$$

This corresponds to a collapsing mixed region that is symmmetric about the plane $x = 0$ and we consider only the right half of it.

The right-hand boundary, $x = X_0$, is taken to be sufficiently far from the origin. For single-wave experiments, the 'outflow' boundary conditions

$$\frac{\partial \psi}{\partial x} = 0, \quad \frac{\partial \omega}{\partial x} = 0, \quad \frac{\partial \rho}{\partial x} = 0 \tag{2.9}$$

are used. For experiments on colliding waves, the 'slip' plane conditions (2.8) are used instead.

Selection of the upper boundary condition is motivated by our interest to simulate deep-water internal solitary waves which are the fastest and the most relevant to the natural environment. To this end, we have considered two types of boundary conditions on the upper wall: a rigid lid 'free-slip' condition

$$\psi = 0, \quad \omega = 0, \quad \rho = -0.5 \tag{2.10}$$

and a 'deep-water' approximation:

$$\frac{\partial \psi}{\partial y} = 0, \quad \omega = 0, \quad \rho = -0.5. \tag{2.11}$$

The suitability of both boundary conditions has been examined in a preliminary numerical study which, in particular, aimed at determining an appropriate range for D such that the results are essentially independent of the selected depth of the computational domain. The numerical study indicated that when using condition (2.10) the results 'converge' for $D > 40$. In particular, for this range of D, the experimental results for the wave speed in deep water are recovered (§ 3.4). On the other hand, when using condition (2.11), we find that a depth $D = 16$ is sufficient to approximate the 'deep-water' case (see § 2.3 below). Since a smaller domain depth translates into a more efficient discretization, selection of condition (2.11) with $D = 16$ is adopted in most of the computations.

2.3. *Numerical method*

The governing equations (2.2)–(2.4) subject to boundary conditions (2.6)–(2.10) are solved using finite-difference schemes. The vorticity transport equation (2.2) is integrated in time using the third-order Adams–Bashforth scheme, while spatial derivatives are approximated using second-order centred differences. The streamfunction Poisson equation (2.4) is discretized using second-order centred differences, and the resulting system is inverted using a fast Poisson solver. The latter is based on performing FFTs of the discrete equations in the z-direction. This leads to a collection of decoupled, tridiagonal systems for individual Fourier modes, which are directly inverted using the Thomas algorithm.

In most laboratory experiments on internal solitary waves, the pycnocline thicknesses are of the order of a few millimetres, and the density difference between the lower (salt water) and the upper (fresh water) fluids is about 0.04 gm cm^{-3}. Thus, using as representative values $\tilde{h} = 5$ mm and $\Delta\tilde{\rho} = 0.04$ gm cm^{-3}, the Reynolds number $Re = \tilde{h}\tilde{U}_c/\tilde{\nu}$ is about 100. This is the Reynolds number value used in most of the present simulations. These are carried out for extended periods (up to 150–200 normalized time units) that are long enough to observe the evolution of the waves as they dissipate their energy. To do so, it is essential to minimize the diffusion rate in the governing equation for the density anomaly, so that the change in the pycnocline thickness, and the impact of this change on wave properties, remain negligibly small. The physical Schmidt number for salt diffusion in water is about 700–800. However, in preliminary tests in which the Schmidt number was systematically varied, we have determined that a Schmidt number value $Sc = 100$ is sufficiently high for density diffusion to be ignored during the simulation period.

The basic computational mesh used in the simulations has 256 points in the vertical direction and 2048 points in the horizontal direction. The grid is used to discretize a domain of length $X_0 = 384$ and height $D = 16$; thus, the grid aspect ratio $\Delta x/\Delta z = 3$.

With this resolution the grid Reynolds number for the vorticity equation (2.2) is about 6. Meanwhile, the grid 'Péclet' number for the density advection equation is about 600. This high value of the grid 'Péclet' number leads to numerical difficulties when integrating the density advection equation using second-order centred differences. These difficulties manifest themselves by the appearance of high-frequency wiggles, which may pollute the entire solution when the wave amplitude is large. To overcome these difficulties, the density advection equation is integrated using an explicit upwind scheme which was developed by Valentine (1987) (see also Valentine & Tannous 1989). The scheme is second-order in space and conservative. The validity of this upwind scheme has been tested against the same integration scheme used for the vorticity transport equation. The tests, conducted at a Schmidt number $Sc = 10$ and a Courant number $\Delta t/\Delta x = 0.05$, reveal that both schemes yield essentially identical predictions.

The selection of the 'baseline' computational parameters mentioned above followed a detailed study of their effect on the computed solution. To this end, the following parameters were systematically varied: the spatial resolution parameters $(\Delta x, \Delta z)$, the time step Δt, and the (artificial) domain depth D. Briefly, the results of the numerical study show that: (*a*) for the above range of values of $(\Delta x, \Delta z, \Delta t)$ the computed solution is essentially independent of the grid size and time step, and (*b*) if not properly selected, the depth D can have a pronounced effect on the predictions. Since the selected value of D significantly affects the computational time, its selection was carefully optimized. While focusing on the peak amplitudes considered in the analysis, D was systematically varied and its effect on the solution was monitored. The results showed that: (i) the numerical solution becomes essentially independent of D as the latter is increased, and (ii) for $D \geqslant 16$ the wave structure is weakly dependent on D and variations of global waves properties such as wave speed and wave length become small (less than 2–3%). Thus, as indicated above, a value of $D = 16$ was selected in production computations.

2.4. *Particle tracking and wave measurements*

For the purpose of flow visualization and measurement of wave properties, the motion of passive particles is also tracked in the computations. The particles are initially distributed in four different 'arrays'. The first array describes particles which, initially, are uniformly distributed within the rectangular mixed region. The second array describes particles which are initially distributed along horizontal lines close to the centreline ($z = 0$). Particles in the third array are initially located on the horizontal line $z = 1$ ($\tilde{z} = \tilde{h}$ in dimensional units). Finally, the fourth array describes particles whose initial locations belong to vertical lines 'downstream' of the mixed region. Typically, the number of particles in the simulation is 200 000. As discussed in the following sections, the computed motion of the Lagrangian particles allows us to perform a detailed visualization of the flow. In addition, the particle motion also simplifies measurement of some wave properties, as discussed below.

The basic parameters measured in all the numerical experiments are illustrated in figure 2. The amplitude and wavelength of a wave are defined in accordance with the weakly nonlinear theory (Benjamin 1967; Davis & Acrivos 1967). The wave amplitude, a, is defined as the maximum displacement of the $\psi = 1$ streamline. The wavelength, λ, is defined as the half-width of the wave at $z = 1 + a/2$. Both the wave amplitude and wavelength are measured using the recorded positions of particles initially placed on the line $z = 1$. Since the wave does not exhibit fore-aft symmetry, the measurements are restricted to the forward portion of the wave. The wave position, x_w, is recorded

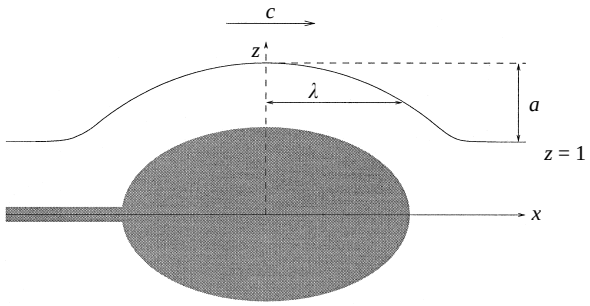

FIGURE 2. Basic parameters for solitary waves measured in the simulations. The normalized wave amplitude, a, is determined from the maximum displacement of particles initially located on the line $z = 1$. The wavelength, λ, is the half-width of the wave at $z = 1 + a/2$.

every few computational time steps, as well as the location of the foremost point of the intrusional bulge, and the length, L_b, and height, H_b, of the bulge. The wave speed can be accurately computed from these measurements, for both small- and large-amplitude waves.

3. Results of numerical experiments

3.1. *Generation and propagation of solitary waves*

As mentioned in the introduction, the collapse of the mixed region leads to an intrusional current and the generation of a train of internal solitary waves. Observations of these phenomena indicate that the general appearance of the intrusional current and wave train depends on the initial height and length of the mixed region. Our observations are based on consideration of a large number of initial conditions, some of which are summarized in table 1. Different runs correspond to different sizes of the initial mixed region, which are arranged in decreasing order. The heights and lengths are varied systematically, with runs 1–5 conducted at $H = 5$, while runs 5–11 are conducted with $L = 10$.

All of the cases considered share a number of similarities. Specifically, in all cases, several solitary waves are observed. The leading wave has the largest amplitude and propagation speed and is followed by the second wave and so on. The wave amplitude and propagation speed decrease with the order of the wave in the wave train. Thus, the distance between the waves gradually increases as they propagate away from the origin. The actual number of waves is determined by the length and height of the mixed region. Unfortunately, the actual number of waves generated during an experiment is hard to determine accurately, as the last waves in the train are very small and hard to distinguish from 'noise'. Since we are primarily interested in the structure of large-amplitude waves, we have not attempted to address this difficulty nor attempted to determine a functional relationship between the actual number of waves generated and the length and height of the mixed region.

When the mixed region is sufficiently large, the intrusion takes the shape of an elliptic bulge which moves with the leading solitary wave. As shown in figure 3, large-amplitude waves transport mixed fluid over a long distance. A thin line of particles emanates from the rear part of the bulge and extends back to the origin. This process is indicative of viscous dissipation (§ 3.6) with corresponding reduction in the size of the bulge.

When the normalized wave amplitude becomes smaller than a critical value, the

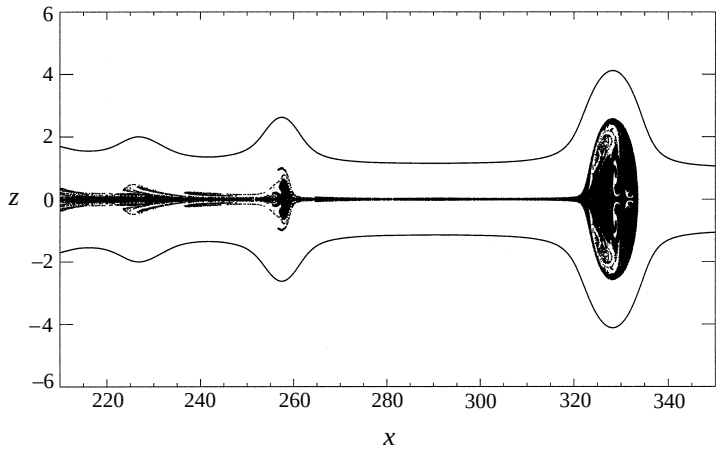

FIGURE 3. The train of large-amplitude solitary waves produced by the collapse of a mixed region with $H = 5$ and $L = 30$. The Reynolds number $Re = 50$ and the Schmidt number $Sc = 200$. The leading wave transports mixed fluid inside; it is followed by smaller waves, which can also transport fluid. The waves gradually separate in space as they propagate away from the origin.

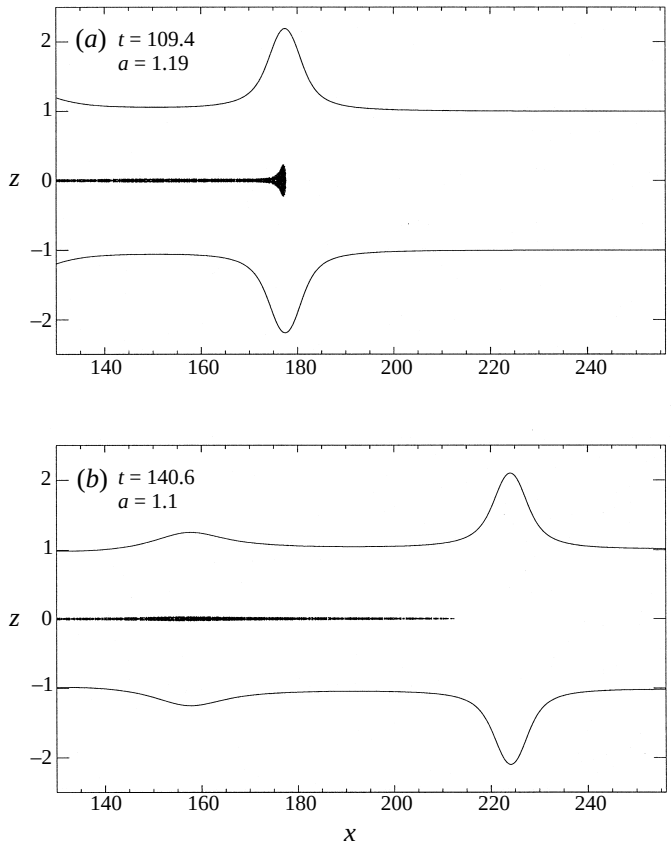

FIGURE 4. Transition from (*a*) a mass-transporting solitary bulge to (*b*) a 'regular' non-mass-transporting wave. The process occurs over some period of time and the critical wave amplitude, at which the intrusion tip is overtaken by the wave crest, $a_c = 1.18$. $Re = 100$ and $Sc = 100$.

Run	H	L	a_{max}	c_{max}	E_0	Comments
1	5.0	40	3.78	2.60	491	
2	5.0	30	3.60	2.57	369	periodic eddy shedding behind
3	5.0	20	3.32	2.48	245	
4	5.0	15	3.08	2.40	186	
5	5.0	10	2.78	2.25	123	
6	4.5	10	2.52	2.15	99	onset of entrainment
7	4.0	10	2.27	2.03	78	
8	3.5	10	2.00	1.91	59	well-defined elliptic bulges
9	3.0	10	1.72	1.77	42	
10	2.5	10	1.41	1.60	28	
11	2.0	10	1.08	1.47	17	non-mass-transporting waves
12	2.0	5	0.93	1.38	9	

TABLE 1. Matrix of initial conditions used in the computations, showing non-dimensional height, H, and length, L, of the initial mixed region. a_{max} is the maximum amplitude of the leading solitary wave, and c_{max} its maximum speed. E_0 is the normalized initial potential energy of the mixed region as defined § 3.3. Unless otherwise stated, all runs are performed with $Re = 100$, $Sc = 100$, $D = 16$, $\Delta x/\Delta z = 3$, and $\Delta t/\Delta x = 0.05$. In all cases, the deep-water boundary condition (2.11) is employed.

wave is no longer able to transport particles, and the intrusion is left behind the leading wave. The intrusion continues to move forward for some time after the leading wave has passed. It gradually comes to rest, acquiring a sharp-nosed form (figure 4). The tip of the intrusion can be moved back and forth by the subsequent passage of the following waves in the train.

The critical wave amplitude is defined as the wave amplitude at which the intrusion tip starts to lag behind the wave crest. Computed results obtained for the conditions listed in table 1 yield a critical wave amplitude $a_c = 1.18$. This value is close to the theoretical estimate of Davis & Acrivos, $a_c = 1.2$, and experimental predictions (Kamachi & Honji 1982). Note that all the conditions of table 1 have $Re = 100$, i.e. the dependence of a_c on Re is not specifically addressed in the present study.

3.2. *Internal wave structure*

As mentioned in the introduction, there is as yet no good understanding of the nature of the flow around and inside internal solitary bulges, especially when these bulges have large amplitudes. Even from a qualitative perspective, our knowledge of the detailed features of the flow is lacking. Thus, the computations are used to visualize the flow for various initial conditions, with particular emphasis on the structure of the solitary bulges. As discussed in further detail below, the computations reveal a variety of different features, depending on the normalized wave amplitude and the Reynolds number.

When the wave amplitude is less than critical, 'regular' waves are observed which do not transport fluid. The flow pattern is similar to that predicted by the weakly nonlinear theory. Specifically, the isopycnal lines are deviated from their equilibrium horizontal positions and baroclinic production of vorticity occurs as a fluid particle is displaced by the incoming wave. The maximum vorticity achieved coincides with the maximum elevation, and starts decreasing afterwards. The streamfunction distribution exhibits closed circulation cells in a stationary frame of reference, whereas open streamlines are obtained in a reference frame moving with the wave (e.g. Kamachi & Honji 1982). Since the structure of these small-amplitude solitary waves is simple, it will not be illustrated here.

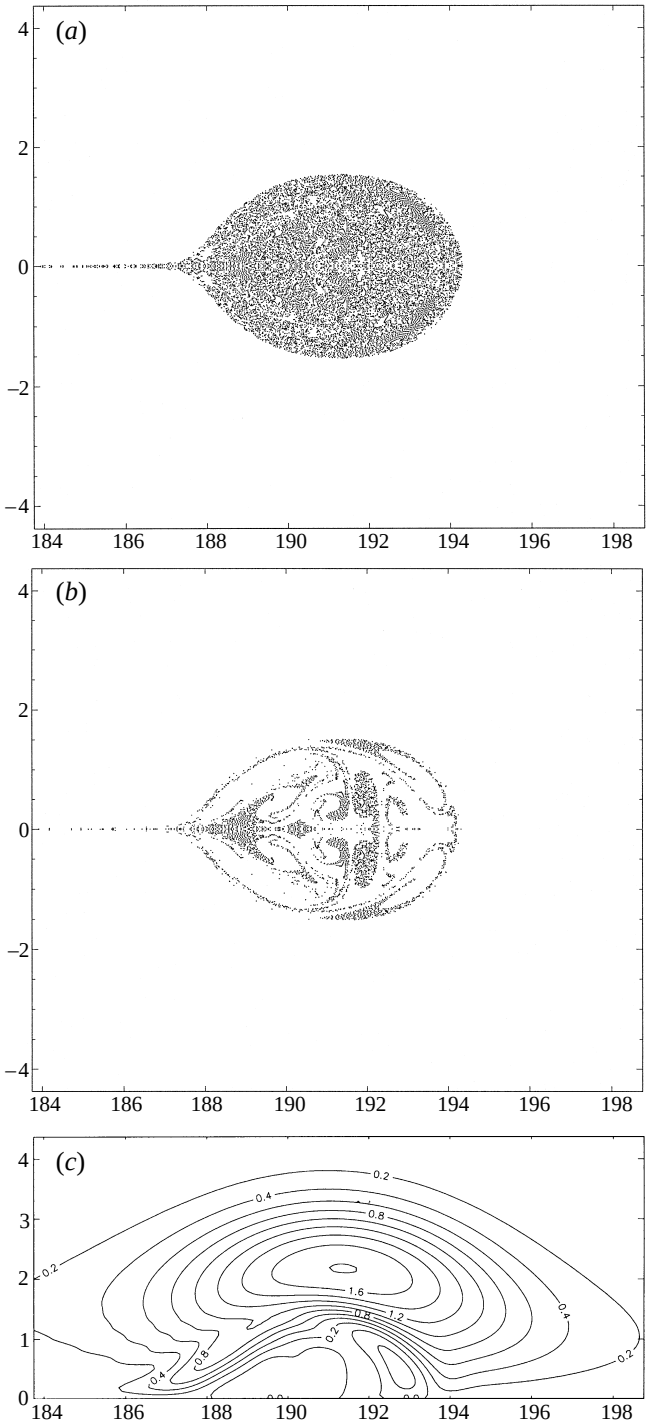

FIGURE 5. (*a*) The leading solitary wave for run 7 in table 1. The wave is visualized at $t = 93.7$ by plotting the Lagrangian particles initially located in the mixed region. The normalized wave amplitude $a = 2.07$ and the bulge has a well-defined elliptic shape. (*b*) The same wave as in (*a*) but only particles occupying the lower half of the mixed region are plotted. (*c*) The distribution of vorticity for the same wave.

As mentioned earlier, waves with amplitudes larger than critical transport fluid particles inside; however, the structure of these waves differs according to the wave amplitude and the Reynolds number. At $Re = 100$ and for wave amplitudes not larger than $a \approx 2.3$, bulges have a well-defined elliptic shape with sharp boundaries (figure 5*a*). These bulges propagate a long distance without entraining fluid from the outside while gradually losing mixed fluid to a thin tail behind. The computations indicate that internal circulation within the bulges occurs. Evidence of this internal circulation is provided in figure 5(*b*), which depicts particles initially located in the lower half of the mixed region prior to collapse. However, this internal circulation is weak, as there is no substantial vorticity inside the bulge. As shown in figure 5(*c*), viscous diffusion leads to a smooth vorticity distribution, with gradual variation across the boundary of the bulge and weak cells of negative vorticity inside.

When the wave amplitude becomes larger than $a \approx 2.3$ (at $Re = 100$), the bulge appearance changes dramatically as entrainment develops. Results obtained by repeating several of the runs in table 1 at $Re = 50$ and $Re = 200$ clearly show that the onset of entrainment is highly senstive to the Reynolds number. Briefly, the higher the Reynolds number $Re \equiv \tilde{U}_c \tilde{h}/\tilde{\nu}$ the lower the wave amplitude at which entrainment develops. This suggests that the condition for onset of entrainment is determined by the effective Reynolds number based on the wave speed and wave amplitude $Re_e \equiv \tilde{c}\tilde{a}/\tilde{\nu}$.

The structure of a bulge with a developed entrainment pattern at $a = 2.2$ and $Re = 200$ is illustrated in figures 6 and 7. In order to clearly identify the mechanism of the entrainment process, figure 6(*a*) shows the instantaneous position of particles originating from the mixed region, while figure 6(*b*) shows particles initially located on the pycnocline as well as on the line $z = 1$. (Note that although only the upper half of the bulge is actually computed in the simulations both the upper and lower halves are shown in the particle plots; however, only the upper half of the structure is discussed.) Figure 6(*a*) shows that the leading part of the bulge has a mushroom-type structure followed by a well-defined lobe; the bulge moves from left to right. The entrainment of particles into this lobe can be discerned by simultaneous examination of figures 6(*a*) and 6(*b*). In particular, figure 6(*b*) shows that particles intially located close to the centreline ($z = 0$) move around the leading part of the bulge and are entrained into the lobe. Once inside the bulge, the entrained particles start moving down towards the centreline. The particles circulate around the lobe, and are then advected into the rear part of the bulge. Eventually, some entrained particles are ejected into the tail of the bulge.

The structure of the bulge shown in figure 6 is further examined in figure 7(*a–d*), which respectively depict contours of vorticity, density, streamfunction in a reference frame moving with the bulge, and streamfunction in a stationary frame. Figure 7(*a*) reveals that the flow outside the bulge is wave-dominated with a strong baroclinic generation of positive vorticity. Within the bulge, one can observe a negative-vorticity cell coinciding with the lobe (see also figure 7*c*). The magnitude of negative vorticity within this cell reaches a substantial fraction (about 40%) of the peak vorticity outside. The generation of negative vorticity is related to the overturning of isopycnals, which results in negative baroclinic torque in the upper plane. The appearance of negative-vorticity cells has been recently observed in laboratory experiments on internal solitary waves (Maderich, van Heijst & Brandt 1996). The sense of rotation within the negative-vorticity cell is clockwise, i.e. opposite to the counterclockwise rotation that one would expect in a vortex pair. Thus, the vorticity structure of bulges computed here differs from that reported in the experimental studies of Kamachi &

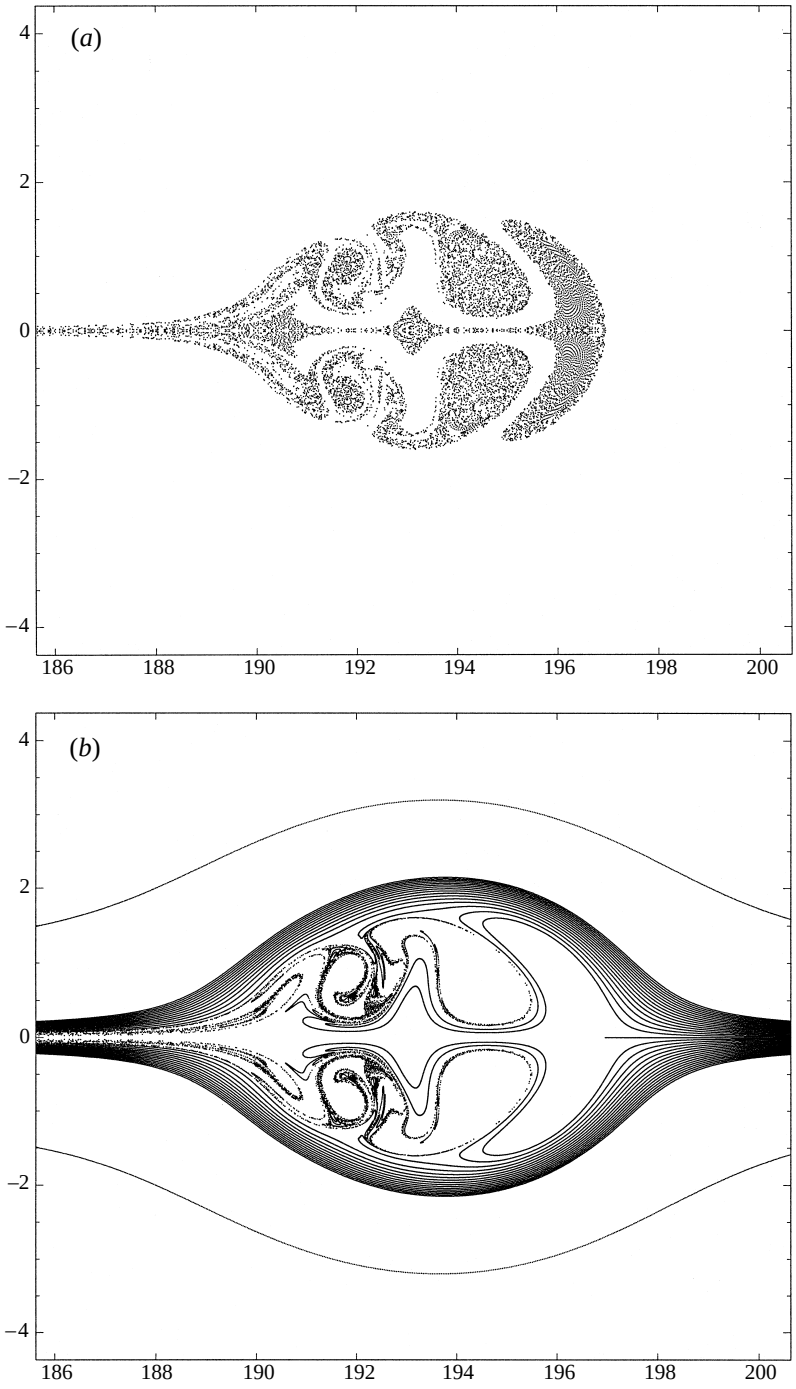

FIGURE 6. The leading solitary wave at the same time and for the same initial conditions as in figure 5 (table 1, run 7) but with $Re = 200$. The wave amplitude $a = 2.2$ is slightly higher than in figure 5 because of larger Re. The entrainment is visualized by plotting (*a*) Lagrangian particles originating from the mixed region and (*b*) particles initially located along the pycnocline and on the line $z = 1$.

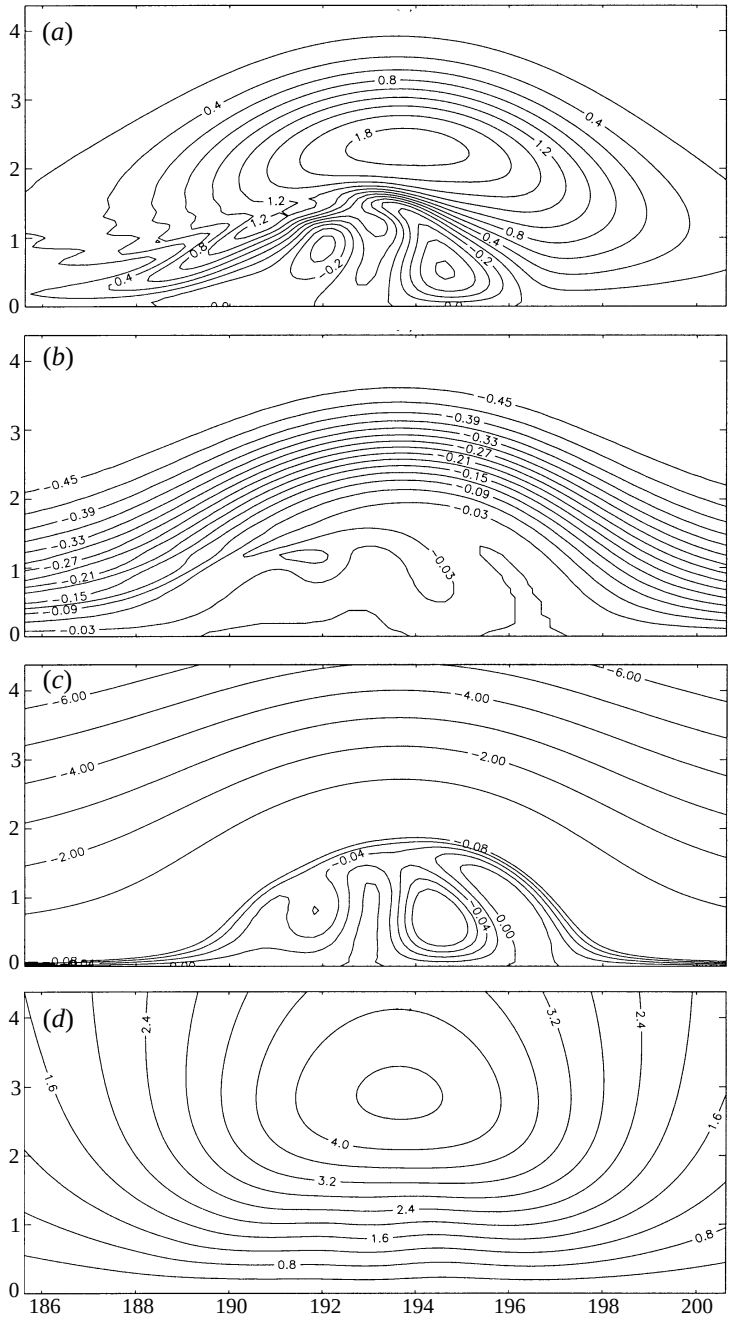

FIGURE 7. Contours of (*a*) vorticity, (*b*) density, (*c*) streamfunction in the reference frame moving with the wave, and (*d*) streamfunction in a stationary reference frame, for the wave of figure 6. Only the upper half of the wave is plotted.

Honji (1982) and of Stamp & Jacka (1995). This difference may be due to the wave generation process. In the present simulations internal solitary waves are generated by the collapse of a mixed region, while in the experimental studies of Kamachi & Honji and Stamp & Jacka the waves are generated by pushing the fluid along the

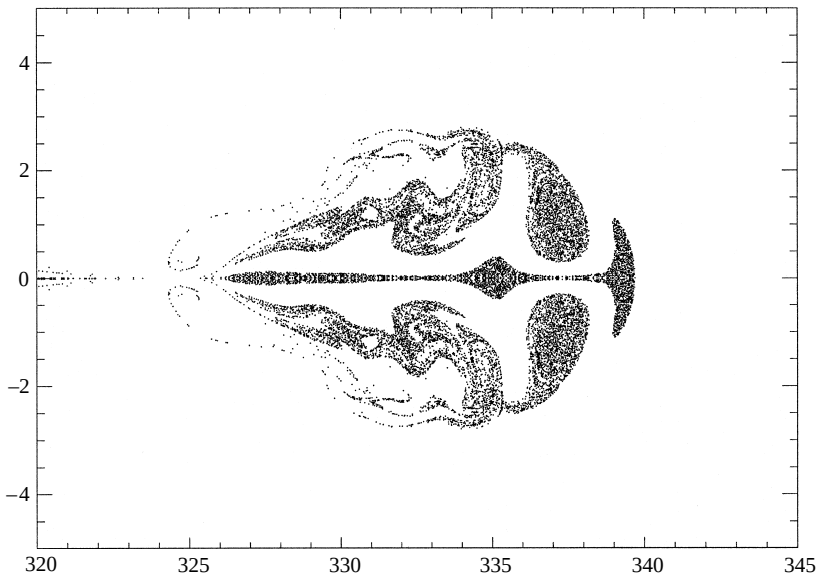

FIGURE 8. The leading solitary bulge for run 2 in table 1. The structure of the bulge is visualized by plotting Lagrangian particles initially located in the mixed region. The plot is generated at $t = 125$; the wave amplitude is $a = 3.43$.

pycnocline. In the latter case, vorticity generated during the flow acceleration phase (positive in the upper half of the wave for waves moving from left to right) may be entrained into the bulge and either prevent the generation of the negative-vorticity cells or hide their presence. Another possibility is that the negative-vorticity cells are actually present in the experiment, but hard to detect using streakline or dye visualization measurements.

Figures 8 and 9 depict the structure of a bulge with large amplitude $a \approx 3.5$ at $Re = 100$. The figures clearly show that as the wave amplitude increases both the structure of the bulge as well as the entrainment pattern become significantly more complex. The leading part of the bulge still maintains a mushroom-like structure, but is narrower and shorter than the bulge amplitude. The elevation at which particles start being entrained into the bulge is thus closer to the centreline and the entrainment process is more intense. The figures also indicate that mixing in the rear part of the bulge also increases. Another distinctive feature of large-amplitude bulges is the periodic shedding of vortices behind the bulge. This shedding is clearly illustrated in figure 9(a, b) which depicts the location of Lagrangian particles originally located along horizontal lines outside and 'downstream' of the mixed region. The formation of these eddies is reminiscent of Kelvin–Helmholtz vortices and their presence indicates that the vorticity layer at the boundary of the bulge is unstable. These vortices also entrain fluid, both from within the bulge and from the outside. As the vortices are shed behind the bugle, small 'droplets' are occasionally entrained into the rear part of the bulge and carried for a long distance before being ejected (figure 9a, b). For medium wave amplitudes, the shedding of vortices from the boundary of the bulge has a transient nature: it occurs just after the wave formation and then stops a while later.

The eddy shedding behind large-amplitude bulges explains a curious and puzzling

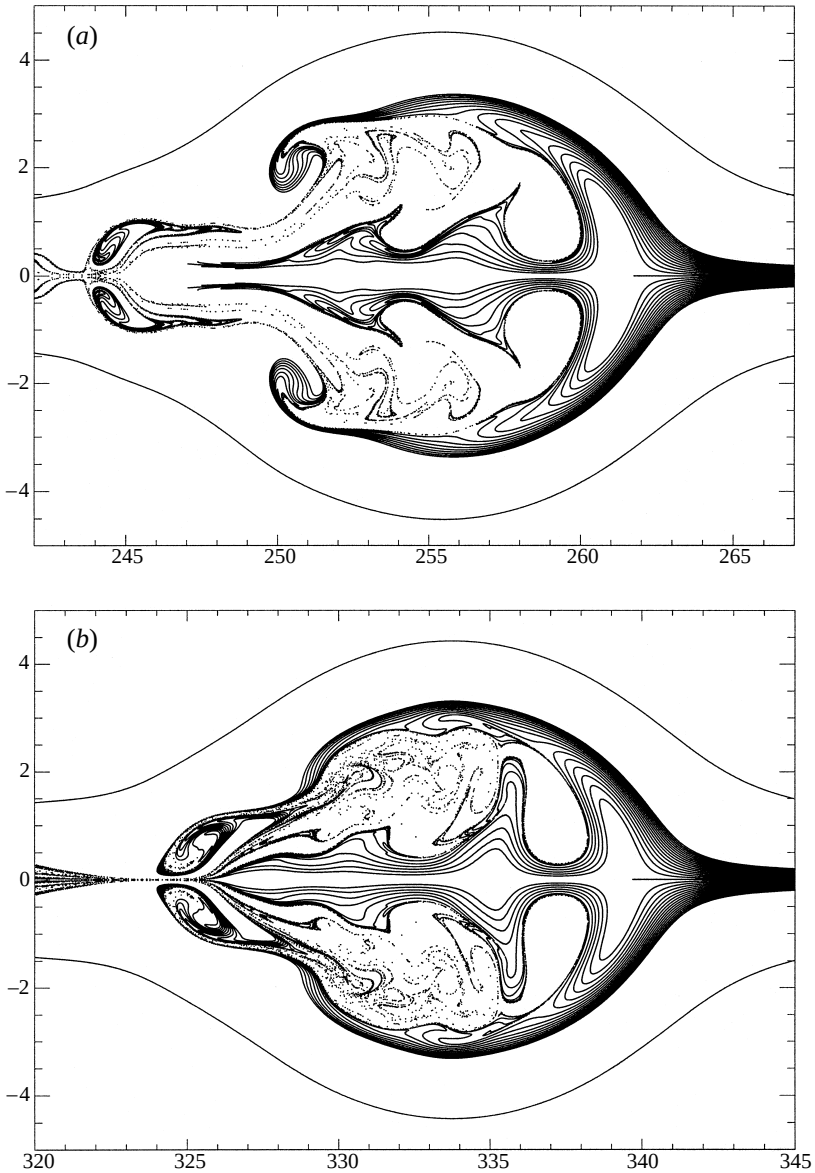

FIGURE 9. The structure of the leading solitary wave for run 2 in table 1, visualized by plotting Lagrangian particles initially located on the pycnocline and on the line $z = 1$. The frames are generated at (*a*) $t = 93.75$ and (*b*) $t = 125$. The corresponding wave amplitudes are $a = 3.51$ and $a = 3.43$, respectively.

observation in dye visualization experiments† which show that following the passage and decay of the waves the dye (initially confined to the mixed region) becomes distributed along fine, distinct, horizontal layers. If undisturbed, this fine layered

† One of the authors, D. Terez, participated in laboratory experiments and visually observed the fine structures after the passage of internal solitary bulges. However, it is very difficult to make good quality photographs of these layers and to our knowledge no such photographs are reported in a literature.

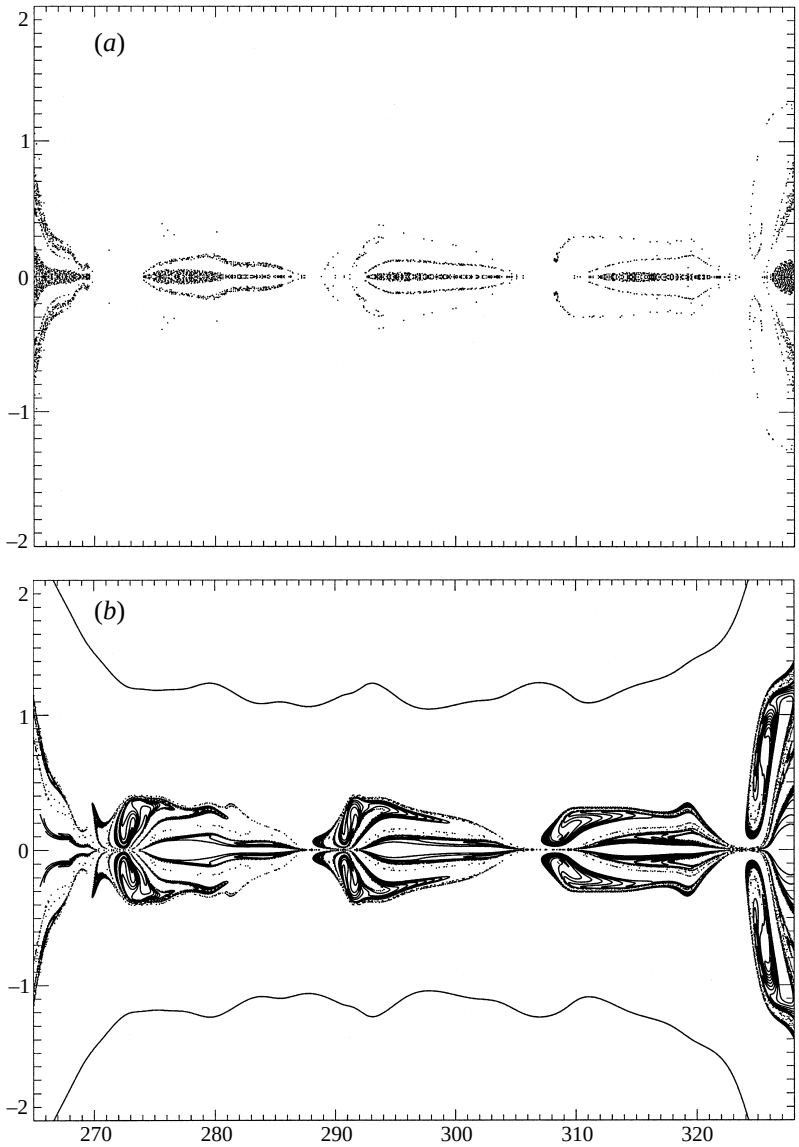

FIGURE 10. The wake of the leading solitary bulge of figure 8, visualized by plotting (*a*) particles initially located in the mixed region, and (*b*) particles initially located along the pycnocline. The plots extend from the rear part of the leading wave to the leading part of the second wave in the train.

structure can persist for several hours after the experiment is over. The origin of this phenomenon can be directly traced to the eddy shedding behind the bulge, as illustrated in figures 10(*a*) and 10(*b*). The figures show three structures which are nearly equally spaced between the leading and second solitary waves. Figure 10(*a*) reveals a thick tail around the centreline and two thin layers of particles in the upper half-plane. Particles in these thin layers originated in the mixed region, were transported by the bulge and later ejected into its wake. Some of these layers will be disturbed in the vertical direction due to the passage of subsequent waves of smaller

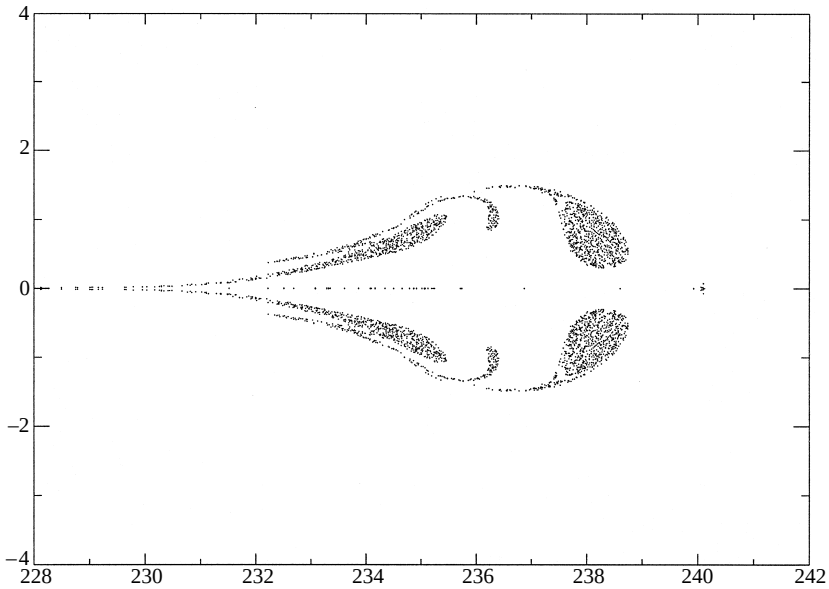

FIGURE 11. The structure of the leading solitary wave generated by the collapse of a partially mixed region. The plot shows the location of Lagrangian particles originating from the mixed region.

amplitude; others will be entrained in the following bulges, which may also trigger a similar mechanism.

We finally note that in the computational experiments discussed above the internal solitary waves are generated by the collapse of a rectangular *uniformly* mixed region. Computational experiments with partially mixed collapsing regions produce bulge structures similar to those shown above, but also reveal some differences. We briefly illustrate potential differences by plotting in figure 11 the structure of a solitary bulge generated by the collapse of a linearly stratified 'mixed region' with a 20% difference in density anomaly between lower and upper parts. The partial mixing leads to a gradual replacement of fluid within the bulge by fluid particles located close to the pycnocline. As a result, a 'double-nosed' structure is formed, as often observed in dye visualization experiments (e.g. Maxworthy 1980). Double-nosed bulges can also lead to the formation of thin horizontal layers of particles, as can be seen in figure 11.

It is interesting to point out that the broad features of the double-nosed bulge are similar to those of the bulges in figures 6 and 8. A distinctive feature, however, is that the mushroom structure at the front of the bulges of figures 6 and 8 is not observed in the bulge of figure 11. In this regard, the doubled-nosed bulge of figure 11 exhibits a greater resemblance to experimental observations. Thus, the leading mushroom appears to be a delicate feature of two-dimensional, symmetric, collapsing regions, which may be difficult to observe experimentally. We have just noted that slight stratification within the mixed region can cause the disappearance of the mushroom, and had noted earlier that enhanced mixing leads to a reduction in its size. In physical experiments, three-dimensional motion, non-Boussinesq effects and slight asymmetry about the axis may also prevent the formation of the mushroom or lead to its rapid disappearance. On the other hand, the other features of the computed bulges, particularly their lobed structure, appear to be more 'robust' and less sensitive to changes in initial data.

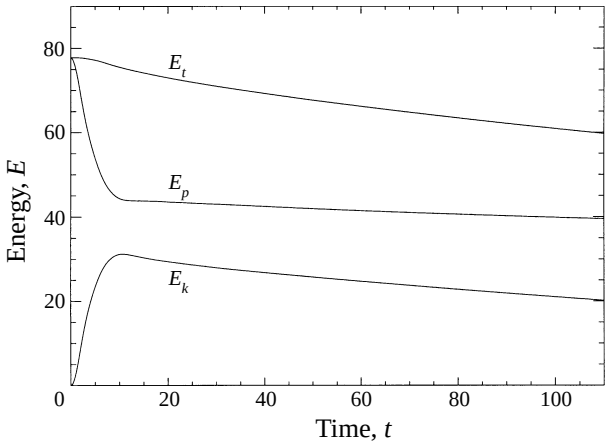

FIGURE 12. Evolution of potential, kinetic and total energy in run 7 of table 1.

3.3. *Energy budget*

At the start of the simulation there is no motion in the entire domain, but the mixed region has some excess potential energy over the surrounding fluid. When it is allowed to collapse part of this potential energy is rapidly converted into kinetic energy of solitary waves and then gradually dissipated.

In the approximation of small relative density variations the kinetic energy within a volume $\mathscr{V}$ can be defined as

$$\tilde{E}_k = \int_{\mathscr{V}} \frac{\tilde{\rho}_0 (\tilde{u}^2 + \tilde{v}^2)}{2} \, \mathrm{d}V. \tag{3.1}$$

A dimensional potential energy can be likewise defined:

$$\tilde{E}_p = \int_{\mathscr{V}} (\tilde{\rho} - \tilde{\rho}_0) \, \tilde{g} \, \tilde{z} \, \mathrm{d}V - \tilde{E}_0, \tag{3.2}$$

where $\tilde{E}_0$ is the reference potential energy corresponding to the undisturbed pycnocline density distribution only. Normalizing the above definitions using the reference velocity in (2.5), equations (3.1) and (3.2) respectively take the following form:

$$E_k \equiv \frac{\tilde{E}_k}{\epsilon} = \frac{1}{2} \int_{\mathscr{V}} \frac{u^2 + v^2}{2} \, \mathrm{d}V \, , \tag{3.3}$$

$$E_p \equiv \frac{\tilde{E}_p}{\epsilon} = 2 \int_{\mathscr{V}} \rho \, z \, \mathrm{d}V - E_0 \, , \tag{3.4}$$

where

$$\epsilon \equiv \frac{\Delta\tilde{\rho} \, \tilde{g} \, \tilde{h}}{2} \tag{3.5}$$

is our reference unit for energy. As can be easily seen, ϵ is the work required to raise a unit volume of interfacial fluid by a unit height, which in our case is the thickness $\tilde{h}$ of the undisturbed pycnocline.

The normalized kinetic energy, E_k, and potential energy, E_p, are computed in the simulations and stored every few computational time steps. A representative case of the evolution of potential, kinetic and total energies in the domain is shown in figure 12. The figure shows that during the collapse of the mixed region, potential

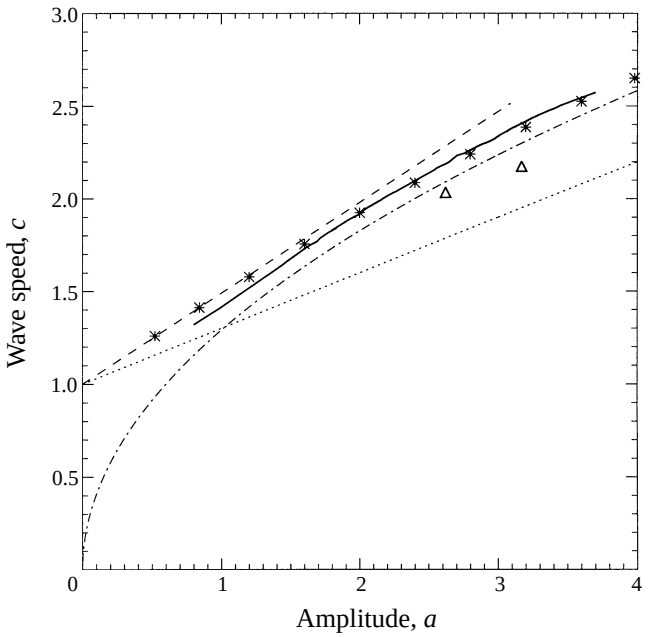

FIGURE 13. Wave speed versus amplitude curves, showing the results of the present simulations (——), the experimental linear fit of Stamp & Jacka (– – – – –), the experimental fit of Maxworthy (*), the results of the weakly nonlinear theory (· · · · ·), and the results of the asymptotic two-fluid solution (3.11) (— · —). The triangles indicate results obtained using the rigid-lid condition (2.10) instead of the deep-water condition (2.11) in otherwise identical simulations.

energy is rapidly transformed into kinetic energy while the total energy decreases only slightly. Following the collapse of the mixed region, both the kinetic and total energies gradually decrease due to viscous dissipation.

One must note that the potential energy computed in the simulations does not represent the available potential energy. In the absence of irreversible diffusive processes, the state with minimium in the potential energy is attained when the mixed fluid is uniformly spread along the centreline. In this case and when the channel has finite length, the potential energy minimum and consequently the available potential energy are well defined. However, in a boundless channel and in the presence of diffusion, it is not clear how to obtain a precise definition of the available potential energy. Diffusion increases the thickness of the pycnocline over long timescales, which reduces the available potential energy. Thus, at large times, diffusion gradually increases the potential energy, E_p, defined in equation (3.4) using a fixed reference state.

Also, it is difficult to associate a precise energy measure with a single solitary wave or bulge. For this reason, we only determine the overall energy within the entire computational domain. The evolution of the total energy during rapid processes is used to examine the overall accuracy of the predictions. An example is provided in § 4 which shows that, during wave collisions (figure 17*c*), the total energy is nearly conserved, while rapid transformation between potential and kinetic energies occurs.

3.4. *Wave speed*

In all of our simulations, the speed of the leading solitary wave is measured and periodically recorded. Figure 13 shows the computed wave speed plotted against wave amplitude, together with available experimental results and theoretical estimates. The

experimental results shown in figure 13 include the linear best fit

$$c = 1 + 0.49\,a\,, \tag{3.6}$$

obtained by Stamp & Jacka (1995) for the range of wave amplitudes $0.1 < a < 3.1$. Also shown is the quadratic relationship

$$c = 1 + 0.51\,a - 0.024\,a^2\,, \tag{3.7}$$

obtained by Maxworthy (1983). Since it closely agrees with our numerical calculations, Maxworthy's relationship is represented with asterisks.

At small amplitudes, the computed wave speed and the experimental data approach the linear wave speed limit. For moderate wave amplitudes, a nearly linear wave speed amplitude dependence is observed; the slope of the curve is significantly higher than that predicted by the weakly nonlinear theory of Benjamin (1967):

$$c = 1 + 0.3\,a. \tag{3.8}$$

Figure 13 shows a close agreement between our computed results and the experimental best fits, especially that obtained by Maxworthy (1983) based on experiments on internal solitary Kelvin waves.

It is interesting to note that there are differences between the two experiments, and also between experiments and the present computations, as far as the wave generation process is concerned. As discussed in § 3.2, the wave generation process may affect the internal bulge structure but, as shown in figure 13, does not appear to influence the wave speed. This suggests that the wave speed and wavelength (§ 3.5) are predominantly governed by the general structure of the stratified flow around the bulge and not very sensitive to its internal structure.

For very large wave amplitudes, $a > 3$, the computed results gradually deviate from linear behaviour. This deviation is not surprising since one would expect that for large wave amplitudes stratification would be confined to a relatively thin layer whose thickness is much smaller than the size of the bulge. In this limit, a two-fluid description of the flow is appropriate. A theoretical two-fluid solution relevant to the present problem is available from the study of Kozlov & Makarov (1990) who analyse steady-state detached gravity currents propagating in a fluid of lesser density. The inviscid solutions obtained by Kozlov & Makarov, which correspond to the asymptotic limit of the two-fluid solitary wave solutions of Pullin & Grimshaw (1988), yield bulges with no relative motion inside and irrotational flow outside. These bulges, also called 'solidons', have self-similar shape with the height to length ratio

$$\alpha \equiv \frac{\tilde{A}}{2\tilde{S}} = 0.232. \tag{3.9}$$

Based on a dimensional argument, the speed of propagation of the 'solidon' must have a square-root dependence on its linear size $\tilde{S}$,

$$\tilde{U} = \beta \left(\frac{\delta\tilde{\rho}}{2\tilde{\rho}} \tilde{g} \tilde{S} \right)^{1/2} \tag{3.10}$$

with $\beta = 0.622$ computed by Kozlov & Makarov. Note that for the limiting two-fluid case, the appropriate lengthscale is the length or height of the solidon. Nonetheless, we can rescale equation (3.10) with respect to $\tilde{h}$ and $\tilde{U}_c$ to get a non-dimensional

propagation speed c as a function of a non-dimensional amplitude a:

$$c \equiv \frac{\tilde{U}}{\tilde{U}_c} = \frac{\beta}{\alpha^{1/2}} a^{1/2}. \tag{3.11}$$

This formula is valid only asymptotically at very large amplitudes, a situation in which the definitions of bulge height and wave amplitude are practically identical. The asymptotic curve given in equation (3.11) is plotted in figure 13, and extended to low amplitudes only to illustrate the square-root behaviour. The asymptotic curve highlights the trend at very large amplitudes, but is not used in a quantitative comparison with the computations in the amplitude range considered here.

Note that figure 13 also provides wave speed predictions obtained using the rigid-lid condition (2.10) instead of the 'deep-water' condition (2.11) in otherwise identical simulations. The results illustrate our earlier discussion of the conditions on the upper boundary, and are representative of the fact that unless large depths are used the rigid-lid condition tends to under-predict the speed of deep-water waves.

3.5. *Wavelength*

For solitary waves, balance between nonlinearity and dispersion is achieved only for a particular relationship between wavelength and wave amplitude. For deep-water internal solitary waves, the wavelength–amplitude scaling predicted by the weakly nonlinear theory is given by (Benjamin 1967)

$$\lambda = 5 / 2a. \tag{3.12}$$

As discussed in the previous section, the predictions of the weakly nonlinear theory are restricted to small amplitudes and are not expected to hold for mass-transporting bulges. Stamp & Jacka (1995) provided a linear best fit to their data,

$$\lambda = 0.95 + 2.1\, a. \tag{3.13}$$

The experimental measurements exhibit large scatter, on the order of 30–40%. In addition, due to large measurement error wavelength estimates were not obtained for small-amplitude waves, and the linear best fit is restricted to the range $1 < a < 3.1$. Both the experimental fit and the weakly nonlinear prediction are plotted in figure 14 along with computed results.

The results shown in figure 14 indicate that for wave amplitudes below critical, the wavelength decreases with increasing wave amplitude. This result is in accordance with the predictions of the weakly nonlinear theory. The computed wavelength reaches a minimum around the critical wave amplitude and then starts increasing, and crosses the experimental best fit at $a \sim 1.5$. Thus, for small to moderate wave amplitudes, the wavelength–amplitude scaling does not exhibit a linear self-similar behaviour, in contrast to the argument by Stamp & Jacka. On the other hand, for large-amplitude waves, figure 14 indicates that a linear behaviour is approached (Kozlov & Makarov 1990; Pullin & Grimshaw 1988). In accordance with the discussion of the previous section, self-similarity, with a corresponding linear wavelength–amplitude scaling, appears to be approached for very large wave amplitudes only.

3.6. *Wave attenuation*

As the wave propagates away from the origin, it gradually loses its momentum and energy due to dissipation phenomena. Consequently, the wave amplitude also decreases with time. One of the goals of the simulations is to determine the character of wave attenuation and to measure the attenuation rate for waves with different

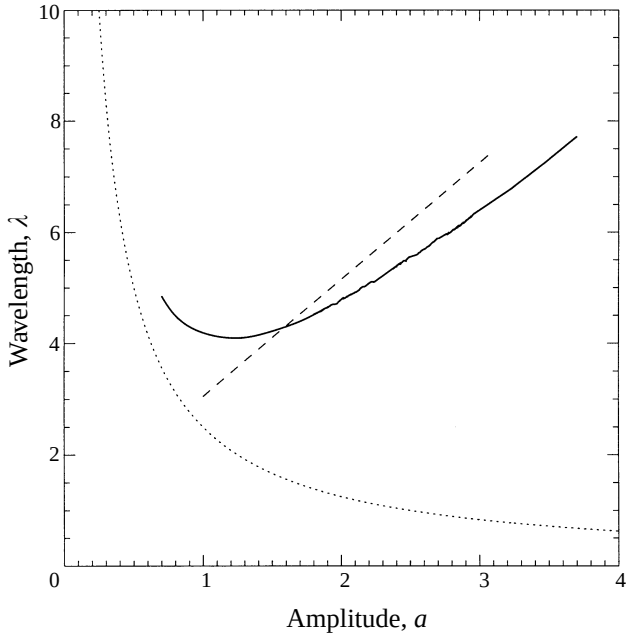

FIGURE 14. Wavelength versus amplitude curves, showing the computed results (——), the experimental linear fit of Stamp & Jacka (– – – – –), and the results of the weakly nonlinear theory (· · · · ·).

amplitudes and for different Reynolds numbers. To this end, computations are carried out in a long domain and for extended time periods.

Figure 15(*a*) shows the evolution of the amplitude of the leading wave at times where dissipation occurs. Included in the figure are runs with different mixed regions and Reynolds numbers. In all the cases computed, the wave amplitude decreases linearly with time. This result is not in agreement with Stamp & Jacka's interpretation of their experimental data which suggests that the wave amplitude decays linearly with position. Note, however, that when appropriately rescaled with respect to the Reynolds number, the computed wave attenuation rates are in agreement with Stamp & Jacka's experimental estimates. The difference between the computational results and Stamp & Jacka's interpretation thus appears to be due to a somewhat large scatter in the experimental data.

The attenuation rate, defined as the slope of the amplitude curve, is plotted in figure 15(*b*). The figure shows that, for a fixed value of the Reynolds number, the amplitude attenuation rate is practically independent of the wave amplitude. Thus, the amplitude evolves according to

$$\frac{\mathrm{d}a}{\mathrm{d}t} = \text{const.} \tag{3.14}$$

Meanwhile, runs performed with $Re = 50$ and $Re = 200$ indicate that the attenuation rate is inversely proportional to the Reynolds number. This suggests that the wave attenuation rate is directly proportional to the fluid viscosity.

It should be emphasized that the amplitude range in figure 15 extends from small-amplitude waves with a below critical to large-amplitude bulges with a developed entrainment pattern and eddy shedding behind. Recall that for the same amplitude value, the internal wave structure differs according to the Reynolds number which, as

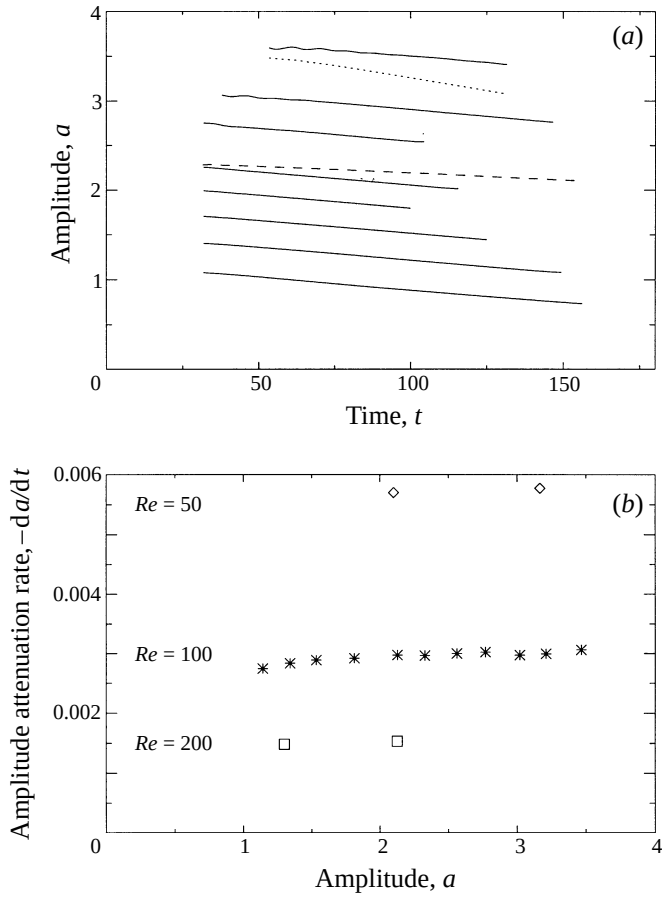

FIGURE 15. (*a*) Evolution of the wave amplitude for different runs: ——, $Re = 100$; – – – –, $Re = 200$; · · · · ·, $Re = 50$. (*b*) Attenuation rate versus wave amplitude for different initial conditions and Reynolds numbers.

noted in § 3.2, can greatly influence the occurrence of entrainment as well. Thus, the present results clearly indicate that for the conditions of the numerical experiments wave attenuation is a purely viscous process that is insensitive to the flow structure. It is possible, however, that for wave amplitudes and/or Reynolds numbers that are larger than those considered here, entrainment and mixing may become more important and significantly affect the wave attenuation rates.

We finally note that the present estimates of waves attenuation rates do not account for some radiative losses. Radiative losses can be caused, for instance, by mode-1 solitary waves that trail the leading bulge and 'drain' energy from it. This situation has been analysed theoretically by Akylas & Grimshaw (1992), and mode-1 waves have been observed in some laboratory experiments (e.g. Stamp & Jacka). Unfortunately, such scenarios are outside the scope of the present simulations, which are based on a symmetric Boussinesq formulation.

4. Wave collisions

One of the interesting properties of solitary waves is their ability to keep their identity after interactions with each other. The remarkable properties of persistence

and self-preservation are common to all types of solitary waves, regardless of the physical system in which they evolve. Since the pioneering work by Zabusky & Kruskal (1965) on nonlinear interactions of solitons, this topic has received considerable attention in the literature. Most theoretical investigations of nonlinear wave–wave interactions are based on analytical or numerical solutions of the weakly nonlinear equations.

Head-on collisions of solitary bulges have been observed in laboratory experiments (Stamp & Jacka 1995; Kao & Pao 1980), but detailed data on the collision events are scarce. Kao & Pao photographed the head-on collision of solitary waves and used the observations to infer that the waves experience a negative temporal phase shift during the collision. Stamp & Jacka also observed head-on collisions of solitary bulges, and provided estimates of wave parameters before and after the collision. They noted difficulties in the measurement of wave properties which lead to large errors in the experimental estimates.

Unfortunately, as mentioned in the previous sections, the weakly nonlinear theory cannot describe large-amplitude mass-transporting waves, which are the subject of the present study. Thus, numerical experiments are performed on the collision of large-amplitude internal solitary waves. Attention is focused on head-on collisions of solitary bulges with the same amplitude; equivalently, the problem can be regarded as the reflection of a single bulge off a vertical slip plane. Numerical experiments on the head-on collision of solitary bulges with different amplitudes have been performed but are not discussed here.

Numerical simulations of head-on collisions of solitary waves are summarized in table 2. For each run the wave position, wave amplitude and wave speed are measured and recorded periodically. The moment of collision is determined from the location of a local minimum on the kinetic energy evolution plot. The properties of the wave before and after collision are reported in the table.

Figure 16 illustrates the head-on collision of two solitary bulges of equal amplitude, $a \approx 2.1$ (table 2, run 2). Only one of the waves is plotted in the figure. The evolution of wave position, wave amplitude and energy for the same run is plotted in figure 17(*a–c*), respectively.

One can see from figure 16, that as the wave approaches the point of collision it changes its shape. At the very moment of collision the wave comes to rest, and the wave amplitude achieves its largest value which is greater than twice its value prior to collision. As shown in figure 17(*c*), the total energy is nearly conserved during the collision event, while rapid transformations between kinetic and potential energies occur. Specifically, at the moment of collision, the kinetic energy reaches its minimum value while the potential energy is maximized. Recall that all of our energy measures are integral quantities over the entire computational domain, and therefore account for contributions from other waves in the train. After the wave amplitude reaches its maximum value, a reflected wave is generated. At some distance from the plane of collision, the reflected wave attains an amplitude that is slightly smaller than that of the incident wave (table 2).

During the collision event, most of the mixed fluid transported by the incident wave is ejected and gradually forms an intrusive current behind (figure 16). Most of the particles carried within the incident bulge are not transported back by the reflected wave. Note, however, that the reflected wave can subsequently entrain and transport particles that originated in the mixed region and were left in the tail of the incident bulge. The present description is in qualitative agreement with the observations of Stamp & Jacka who also report ejection and wave breaking

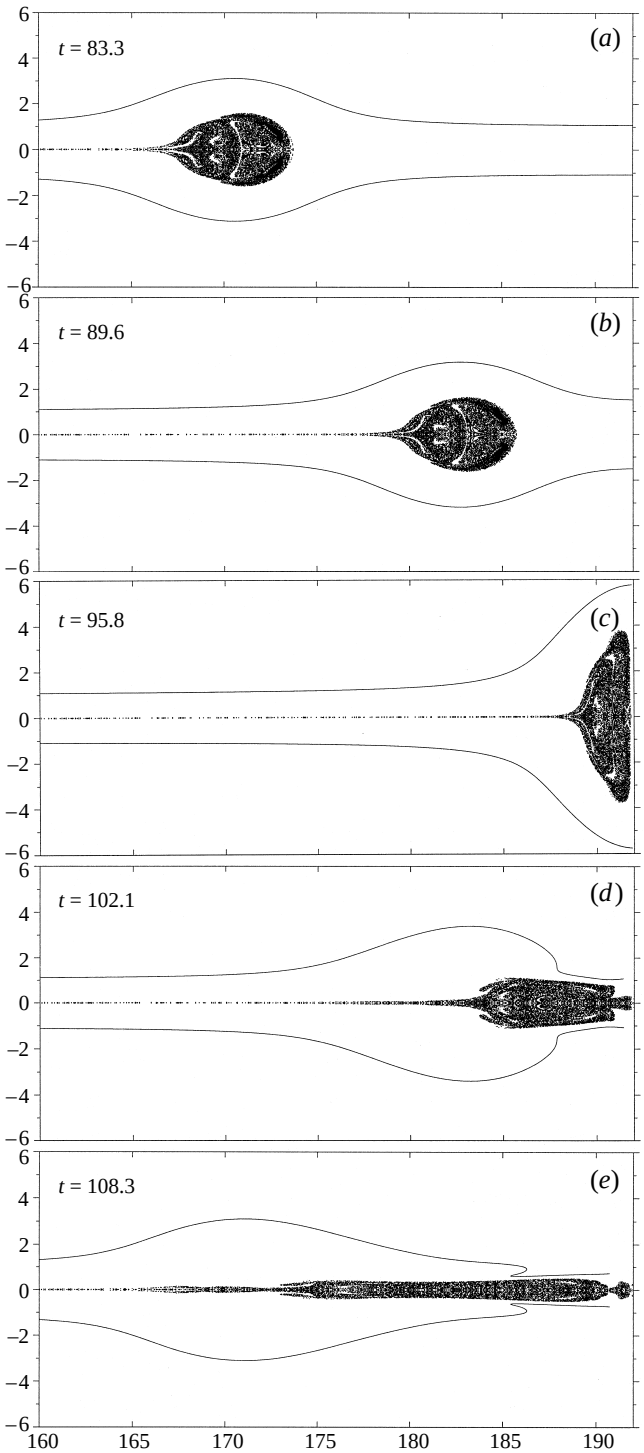

FIGURE 16. Head-on collision of equal-amplitude internal solitary waves from run 2 in table 2. The right-hand boundary of the plots corresponds to the plane of collision. Only one of the waves is shown. The amplitude of the incident waves before collision is $a = 2.11$. The plots show a time sequence of the location of particles initially located in the mixed region and on the line $z = 1$.

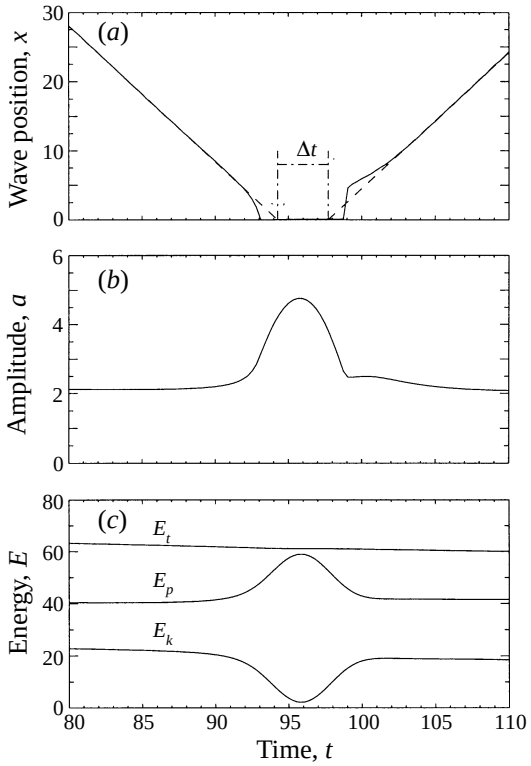

FIGURE 17. The evolution of (*a*) wave position, (*b*) wave amplitude, and (*c*) kinetic, potential and total energy during the collision of figure 16 (run 2 in table 2).

phenomena similar to those depicted in figure 16. However, it differs from their interpretation that the head-on collision of equal-amplitude waves resembles a reflection process and that particles reverse direction along the same path by which they approach.

The pycnocline, on which the reflected wave propagates back from the point of collision, has been changed by the passage of the incident wave and, therefore, is different from its undisturbed state. In particular, the mixed fluid left in the tail of the incident wave makes the pycnocline thicker. We do not attempt to rescale the wave properties with respect to the modified density distribution in the pycnocline. In particular, the amplitude and wave speed values for the reflected wave, listed in table 2, are expressed in terms of the undisturbed pycnocline thickness and the corresponding reference speed.

The increase in the pycnocline thickness partially explains why the reflected wave does not transport as much fluid inside as the incident one. The reflected wave amplitude, rescaled in terms of the new pycnocline thickness, is significantly smaller than the normalized amplitude of the incident wave and thus closer to the critical value. Consequently, the large-amplitude mass-transporting solitary waves do not strictly behave as 'solitons' because they are changed after collisions.

Based on the recorded wave positions before and after collision it is possible to estimate the phase shift suffered by the waves. Both incident and reflected wave trajectories are fitted with straight lines (figure 17*a*). The temporal and spatial phase shifts are then calculated based on the coefficients of the linear fits, with a spatial

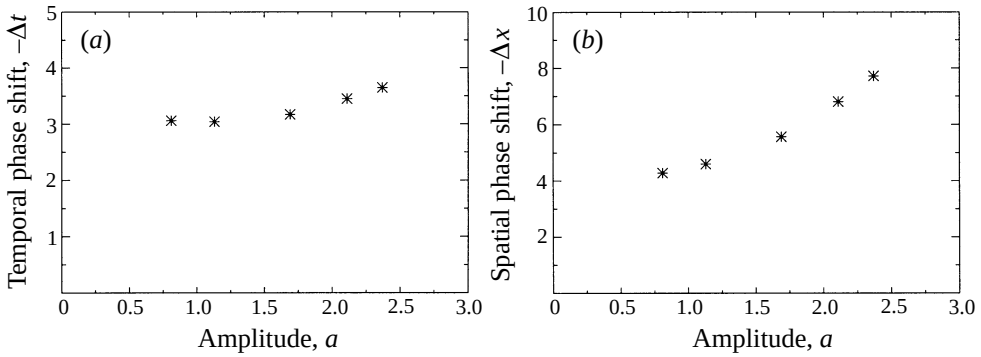

FIGURE 18. (*a*) Temporal and (*b*) spatial phase shifts versus incident wave amplitude.

Run	H	L	a_i	a_r	a_{max}	c_i	c_r	$-\Delta t$	$-\Delta x$
1	4.5	10	2.37	2.36	5.42	2.08	2.11	3.65	7.72
2	4.0	10	2.11	2.08	4.76	1.96	1.96	3.45	6.81
3	3.5	8	1.69	1.63	3.74	1.77	1.76	3.17	5.57
4	3.0	5	1.13	1.01	2.42	1.47	1.51	3.04	4.60
5	3.0	3	0.81	0.71	1.70	1.31	1.39	3.06	4.28

TABLE 2. Collision events between two waves of equal amplitude. H and L are the dimensions of the mixed region, a_i, a_r and c_i, c_r are the values of amplitude and wave speed for the incident and reflected waves, respectively. a_{max} is the maximum wave amplitude achieved during collision. Δt and Δx are the temporal and spatial phase shifts experienced by each wave after the collision. All parameters in the table are normalized in terms of the undisturbed pycnocline thickness, $\tilde{h}$.

phase shift being defined as the product of the temporal phase shift and the speed of reflected wave. The results of the phase shift measurements are summarized in table 2 and plotted in figure 18(*a*, *b*). Both temporal and spatial phase shifts experienced by the wave during the collision are negative, in agreement with the compressible flow computations of Brown & Christie (1994*b*). The temporal phase shift shows only a slight growth with increasing wave amplitude (figure 18*a*), whereas the increase in the spatial phase shift is mainly due to the larger wave speed, and therefore is more pronounced (figure 18*b*). One can see from figure 17(*c*) that the 'hesitation' of the wave during collision is associated with the transformation of the wave kinetic energy into potential energy and back to kinetic energy.

5. Summary and conclusions

Numerical simulations of large-amplitude internal solitary waves on a pycnocline are presented. In all the present computations, the waves are produced from the collapse of a mixed fluid region. The motion is visualized by tracking passive Lagrangian particles, initially located within the mixed region and along the pycnocline. The structure and properties of the internal solitary waves are studied for a wide range of normalized amplitudes, $0.7 < a < 3.8$. Thus, the present computations attempt to provide a 'bridge' between existing experimental results and analytical predictions, including the weakly nonlinear theory and the asymptotic two-fluid solution.

Computed results indicate that small-amplitude waves with $a < 1.18$ do not trans-

port fluid particles and their structure is well described analytically by the weakly nonlinear theory. Waves with medium amplitudes have a well-defined elliptic shape with only a weak recirculation inside the mass-transporting region. At some amplitude, which is dependent on Reynolds number, entrainment develops and changes the appearance of the wave. The entrainment pattern is associated with the vorticity cells inside the bulge with a sense of rotation opposite to that of a vortex-pair type of motion. Thus, the structure of the waves computed here may differ from that inferred in laboratory experiments using different wave generation techniques (Stamp & Jacka 1995; Kamachi & Honji 1982). Computed results show that the magnitude of the inner vorticity cells can reach about 40% of the peak vorticity outside the bulge. The stratified flow outside the bulge is wave-dominated irrespective of the internal bulge structure, with strong baroclinic production of vorticity. The baroclinic vorticity generation leads to the formation of strong outer vorticity cells that enclose the intrusional bulge. At large amplitudes the rear part of the bulge boundary is susceptible to shear-type instability, that results in periodic shedding of vortices behind the bulge.

Global wave characteristics, including wave speed and wavelength, are measured and compared with experimental data, results of the weakly nonlinear theory and asymptotic solutions for a two-fluid model. An excellent agreement is found between computed wave speeds and experimental measurements. It appears that the global wave parameters are in large part determined by the wave-dominated stratified flow outside the bulge and are not very sensitive to the details of the internal bulge structure. In particular, the wave speed and wavelength appear to be influenced primarily by the size of the bulge only. At large amplitudes our computed results show a trend toward the asymptotic two-fluid self-similar solution.

Computed results show that for all cases considered the wave amplitude decreases linearly with time, with an attenuation rate that is inversely proportional to the Reynolds number. This indicates that the dissipation is predominantly viscous at the range of amplitudes and Reynolds numbers studied. However, it is possible that at higher Reynolds numbers the dissipation rate may be substantially influenced by the entrainment and mixing of fluid from the outside, and by ejection of mixed fluid in the tail of the bulge. The present symmetric Boussinesq formulation reproduces only mode-2 solitary waves; therefore, possible mode-1 non-Boussinesq effects are omitted from this study.

Numerical experiments on head-on collisions between equal-amplitude waves reveal that the bulges eject most of the mixed fluid after the collision. Thus, large-amplitude colliding bulges do not, strictly speaking, behave as solitons. The collision event is characterized by rapid transformation between kinetic and potential energies, with the waves practically coming to rest at the very moment of collision. This explains the negative phase shift experienced by the waves during the collision.

We are currently considering several extensions of the present simulations to further quantify the entrainment and mixing associated with large-amplitude bulges, and to more general conditions including the effect of mean shear on the collapse of the mixed region. Other questions which we also plan to investigate are whether bulges with a vortex-pair structure can be generated and whether such structures are stable. The collapse of axisymmetric mixed regions is also being considered.

The authors are grateful to Professor O. M. Phillips for helpful discussions. Computations were performed on an in-house SGI PowerChallenge L, funded by the National Science Foundation under Grant CTS-9509077.

REFERENCES

Akylas, T. R. & Grimshaw, R. H. J. 1992 Solitary internal waves with oscillatory tails. *J. Fluid Mech.* **242**, 279–298.

Amen, R. & Maxworthy, T. 1980 The gravitational collapse of a mixed region into a linearly stratified fluid. *J. Fluid Mech.* **96**, 65–80.

Apel, J. R. 1981 Update: internal waves in the Sulu Sea. *Bull. Am. Met. Soc.* **62**, 1061–1062.

Benjamin, T. B. 1967 Internal waves of permanent form in fluids of great depth. *J. Fluid Mech.* **29**, 559–592.

Brown, D. J. & Christie, D. R. 1994*a* Fully nonlinear solitary waves in the lower atmosphere. In *Proc. 6th Conf. on Mesoscale Processes, Portland, Oregon,* pp. 194–196. American Meteorological Society.

Brown, D. J. & Christie, D. R. 1994*b* Numerical simulations of interacting solitary waves of large amplitude. In *Proc. 10th Conf. on Numerical Weather Prediction, Portland, Oregon*, pp. 235–237. American Meteorological Society.

Christie, D. R. 1992 The morning glory of the Gulf of Carpentaria: a paradigm for non-linear waves in the lower atmosphere. *Austral. Met. Mag.* **41**, 21–60.

Clarke, R. H., Smith, R. K. & Reid, D. G. 1981 The morning glory of the Gulf of Carpentaria: An atmospheric undular bore. *Mon. Weather Rev.* **109**, 1726–1750.

Davis, R. E. & Acrivos, A. 1967 Solitary internal waves in deep water. *J. Fluid Mech.* **29**, 593–607.

Hurdis, D. A. & Pao, H.-P. 1975 Experimental observation of internal solitary waves in a stratified fluid. *Phys. Fluids* **18**, 385–386.

Kamachi, M. & Honji, H. 1982 Steady flow patterns of internal solitary bulges in a stratified fluid. *Phys. Fluids* **25**, 1119–1120.

Kao, T. W. & Pao, H.-P. 1980 Wake collapse in the thermocline and internal solitary waves. *J. Fluid Mech.* **97**, 116–127.

Kozlov, V. F. & Makarov, V. G. 1990 On a class of stationary gravity currents with a density jump. *Izv. Akad. Nauk SSSR, Phys. Atmos. Ocean* **26**, 395–402.

Long, R. R. 1953 Some aspects of the flow of stratified fluids 1. A theoretical investigation. *Tellus* **5**, 42–58.

Maderich, V. S., Heijst, G. J. F. van & Brandt, A. 1996 Laboratory experiments on intrusive flows and internal waves on a pycnocline. *J. Fluid Mech* (submitted).

Maxworthy, T. 1980 On the formation of nonlinear internal waves from the gravitational collapse of mixed regions in two and three dimensions. *J. Fluid Mech.* **96**, 47–64.

Maxworthy, T. 1983 Experiments on solitary internal Kelvin waves. *J. Fluid Mech.* **129**, 365–383.

Ostrovsky, L. A. & Stepanyants, Y. A. 1989 Do internal solitons exist in the ocean? *Rev. Geophys.* **27**, 293–310.

Pullin, D. I. & Grimshaw, R. H. J. 1988 Finite-amplitude solitary waves at the interface between two homogeneous fluids. *Phys. Fluids* **31**, 3550–3559.

Reeder, M. J., Christie, D. R., Smith, R. K. & Grimshaw, R. 1995 Interacting "Morning Glories" over Northern Australia. *Bull. Am. Met. Soc.* **76**, 1165–1171.

Saffarinia, K. & Kao, T. W. 1996 A numerical study of the breaking of an internal soliton and its interaction with a slope. *Dyn. Atmos. Oceans* **23**, 379–391.

Stamp, A. P. & Jacka, M. 1995 Deep-water internal solitary waves. *J. Fluid Mech.* **305**, 347–371.

Tung, K.-K., Chan, T. F. & Kubota T. 1982 Large amplitude internal waves of permanent form. *Stud. Appl. Maths* **66**, 1–44.

Valentine, D. T. 1987 Comparison of finite difference methods to predict passive contaminant transport. *Proceed. ASME Computers in Engng* **2**, 263–269.

Valentine, D. T. & Tannous, A. G. 1989 Calculation of turbulent transport in a rectangular settling tank. *Proc. ASME Conf. Computers in Engineering*, vol. 3, pp. 51–57.

Zabusky, N. J. & Kruskal, M. D. 1965 Interaction of solitons in a collisionless plasma and the recurrence of initial states. *Phys. Rev. Lett.* **15**, 240–243.